Experimental Validation of a Notch-Beam and Frequency-Scanning Sub-THz Radar

Mohammad-Reza Seidi ⓘ, *Graduate Student Member, IEEE*, Armin Karimi ⓘ, *Member, IEEE*,
Alireza Madannejad ⓘ, *Graduate Student Member, IEEE*, Umer Shah ⓘ, *Senior Member, IEEE*,
and Joachim Oberhammer ⓘ, *Senior Member, IEEE*

Abstract—**This article experimentally demonstrates a frequency-sweeping notch-beam sub-THz radar frontend based on a two-line array antenna featuring computational imaging. Operating within 237.5 GHz and 250 GHz with 12.5 GHz bandwidth, the radar utilizes a $12\lambda_c$ delay line to achieve frequency-sweeping capabilities. This configuration allows dynamic notch-beam scanning across angular ranges from $-26.5°$ to $28°$. The radar frontend is highly compact with a total size of 20 mm $\times$ 14.3 mm $\times$ 1.2 mm, including the beam-steering network, a magic-tee for creating the $180°$ phase shift required for creating the notch-beam, and the antenna array, and is implemented by silicon micromachining. The radar was evaluated with single and dual-target scenarios utilizing and benchmarking different computational imaging algorithms, i.e., matched filter (MF), fast iterative shrinkage-thresholding algorithm (FISTA), and multiple signal classification (MUSIC). It was found that the MUSIC algorithm outperforms MF and FISTA in range and angular resolution in single-target scenes, achieving a range resolution of 7.8 mm and an angular resolution of 15.7°, with detection errors of less than 6.6 mm and 3.5°, respectively. Although the MUSIC algorithm maintains reliable range resolution in dual-target scenarios, it performs poorly in providing angular information.**

Index Terms—**Compressed sensing, frequency sweeping, notch-beam, radar, sub-THz.**

I. INTRODUCTION

RADAR systems are critical across various applications, including defense operations, security and concealed weapon detection, automotive safety, and environmental monitoring [1], [2], [3], [4], [5]. Despite their widespread adoption, radar technologies continuously seek advancements in resolution, compact design, and the adoption of adaptive signal processing techniques to navigate the increasing complexities

of modern operational environments. Introducing radars at subterahertz and terahertz frequencies offers a significant advancement, addressing existing challenges by exploiting large bandwidth capabilities [6]. This progress enhances range resolution and contributes to the miniaturization of radar systems, promoting increased compactness and versatility [7]. Conversely, subterahertz frequencies are prone to significant path loss, limiting to short-range applications, and the difficulties of implementing active components and phase shifters at these frequencies restrict the hardware implementations and, thus, the performance.

An innovative beamforming technique, frequency sweeping, has been developed and utilized in many applications because it offers beam-steering at drastically reduced hardware complexity, i.e., not requiring phase shifters, and thus simplifying system architecture and enhancing manufacturability, reliability, and cost efficiency, though at the cost of deteriorating range resolution [8], [9], [10]. [11], [12], [13], [14].

Notch (delta) beam shape has been traditionally used in monopulse radar systems [15]. Due to its sharp-slope radiation pattern, a notch-beam provides higher angular resolution than a broad beam with a wide radiation pattern. In [16], the notch and broad beams for sub-THz radar were conceptually investigated by radar simulations. Their application at sub-THz frequencies exemplifies the utilization of traditional methodologies with modern radar technology exploring new frequency ranges.

Silicon micromachining has emerged as an enabling technology for implementing sub-THz and THz components. This technique enables the fabrication of waveguide components with micrometer-size features, high production uniformity, and, in contrast to other fabrication techniques such as CNC milling and additive manufacturing, offers high volume-manufacturability [17]. Surface roughness in the order of a few nanometers can be achieved by silicon micromachining, superior to any other fabrication techniques, leading to the lowest insertion loss waveguides reported in the literature [18]. Many silicon micromachined components operating at the sub-THz frequencies are successfully demonstrated in the literature [19], [20], highlighting the outstanding potential of silicon micromachining to implement integrated systems in this frequency range [20].

Utilizing unconventional radiation patterns, including notch-beam shape, requires advanced signal processing for target detection and localization. The sophistication of signal processing algorithms is paramount in the efficient detection and

localization of targets. Among these, the multiple signal classification (MUSIC) algorithm and fast iterative shrinkage-thresholding algorithm (FISTA) are noteworthy for their advanced capabilities in estimating signal direction of arrival and reconstructing sparse signals from limited data, respectively [21], [22]. These algorithms leverage the high-resolution potential of sub-THz radar technology and communication to enhance computational imaging performance [23], [24], [25], [26], [27], [28].

This article evaluates a minimalistic radar frontend's potential in single and dual-target image reconstruction scenarios. It investigates the array's ability to detect and localize targets using frequency-steering notch-beam in experimental scenarios, comparing matched filter (MF), FISTA, and MUSIC algorithms. A potential application of the minimalistic antenna frontend includes in-cabin car radar applications for driver and passenger monitoring, fast and efficient airbag triggering, and left kids or pets in the car which in recent years has attracted a lot of attention.

II. FREQUENCY-SWEEPING NOTCH-BEAM SCANNING CONCEPT AND IMPLEMENTATION

A. Frequency-Sweeping Notch-Beam Scanning Concept

The most straightforward approach to create a steerable notch-beam by frequency-sweeping is to utilize a two-element antenna array with out-of-phase excitation signals, in which the beam-steering is achieved by adjusting the phase of each antenna element. In contrast to conventional complex beam-steering techniques utilizing individual antenna-element phase shifters, this approach realizes the required phase shift for beam-steering by two delay lines with different lengths in the feeding network connected to each antenna element. The length difference between the delay lines results in a linear relationship between each antenna's frequency and input phase. The principle for the discussed two-element frequency-sweeping array is depicted in Fig. 1. As demonstrated in the figure, increasing the operation frequency increases the phase difference between the antenna elements. This frequency-dependent phase difference, $\Delta\Phi(f)$, between antennas 1 and 2, is instrumental in steering the beam by frequency sweeping. Despite the array's relatively small aperture of $1.25\lambda_c$—where λ_c is the wavelength at the center frequency—and the physical antenna separation, D, of $0.75\lambda_c$, employing two open-ended waveguide radiators and the delay line length difference of $12\lambda_c$ offers a steering range of $\pm25°$, as shown in Fig. 4.

Given the two-element array as a pair of point-source antennas spaced by distance D with a phase difference $\Delta\Phi$, the total radiated field in direction θ (the counterclockwise angle from antenna 2 to antenna 1 as shown in Fig. 1), at a distance r in the far-field of the array, is given by

$$E = E_0\, e^{+j\Psi/2} + E_0\, e^{-j(\Psi/2-\Delta\Phi)} \tag{1}$$

where the first and second terms in (1) represent the field component due to antenna 1 and antenna 2, respectively, E_0
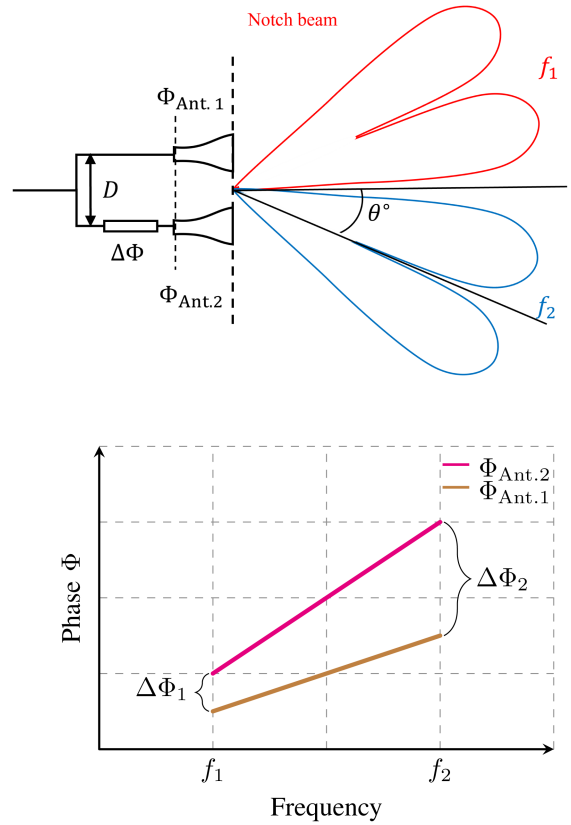

Fig. 1. Illustration of the notch-beam shape for a two-element antenna array, steering the beam by sweeping the operation frequency. Illustration of the frequency-dependent phase shift due to different-length delay lines in the feed network, leading to the frequency beam-steering.

is a constant amplitude, and Ψ is defined as

$$\Psi = kD\sin(\theta) = \frac{2\pi D}{\lambda}\sin(\theta) \tag{2}$$

k, the free-space wavenumber, is equal to $\frac{2\pi}{\lambda}$, in which λ is the operating wavelength in free space and is different from λ_c, which is the wavelength at the center frequency. The phase difference can be calculated as

$$\Delta\Phi = \frac{2\pi}{\lambda_g} \times 12\lambda_c \tag{3}$$

where λ_g refers to the guided wavelength. As a result, (1) can be rewritten as

$$E = 2\, E_0\, e^{j\Delta\Phi/2} \cos(\Psi/2 - \Delta\Phi/2) \tag{4}$$

using trigonometric identities, further simplified (1) to

$$E = 2\, E_0\, e^{j\Delta\Phi/2} \cos\left(\frac{\pi D}{\lambda}\sin(\theta) - \frac{\pi \times 12\lambda_c}{\lambda_g}\right) \tag{5}$$

highlighting the significant influence of the delay line's length difference on the beam steering.

In addition to target localization, two essential performance metrics of a radar system are range and angular (cross-range) resolution, which is the capability of discriminating targets close to each other. Different strategies are commonly employed to

TABLE I
ALGORITHMS' RANGE AND ANGLE DETECTION ERRORS FOR SINGLE-TARGET SCENARIOS

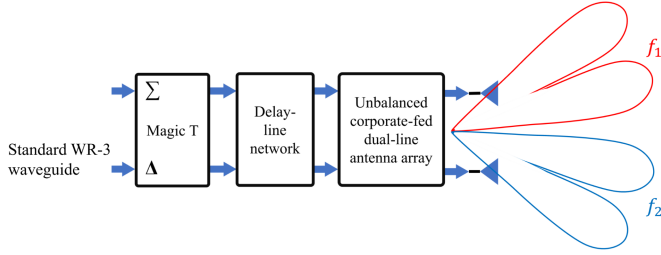| Parameters	Algorithms	Scenario 1	Scenario 2	Scenario 3
Range error (δR mm)	MF	2	0	2
	FISTA	6.6	0	1.6
	MUSIC	6.6	0	1.6
Angle error (δθ°)	MF	0.6	13	2
	FISTA	0.6	12.5	1.5
	MUSIC	3.5	2	1.1

Fig. 2. Block diagram of the radar frontend showing different components in the signal chain and the frequency beam-steering.

enhance the angular resolution of a radar system, such as increasing the size of the antenna aperture or incorporating advanced signal processing algorithms with simple antenna arrays. The relationship between range resolution and system parameters can be described as follows [29]:

$$\Delta R = \frac{c_0}{2 \, \text{BW}_{\text{eff}}} \qquad (6)$$

where ΔR is the range resolution, c_0 is the speed of light in free space, and BW_{eff} is the effective bandwidth on target. Due to the nature of frequency-sweeping beam scanning, the effective bandwidth on the target is narrower compared to the total bandwidth of the system. The effective bandwidth on the targets could be calculated as

$$\text{BW}_{\text{eff}} = \frac{\text{HPBW}}{\text{Scanning span}} \text{BW}$$

where the HPBW is the half power beamwidth ($30° \pm 2°$) of the peaks and the scanning angle is the span for scanning notch beam ($54.5°$), and the BW is the total available bandwidth of the system (12.5 GHz). In addition, the angular resolution of the notch beam corresponds to the HPBW of the notch. The HPBW ($= 30° \pm 2°$) is determined from the two peaks of the notch beam. As shown in Fig. 4, the amplitudes of these peaks vary with scanning, making it challenging to formulate a precise angular resolution. As can be observed, a larger bandwidth contributes to better range resolution, which is grounded in the Fourier transformation principles.

B. Implementation of Beam-Steering Frontend

A block diagram of the implemented frequency-sweeping notch-beam radar frontend, featuring two line array antennas, is shown in Fig. 2. The hardware is discussed in detail in [10] and [12] and briefly summarized here. Creating the notch radiation pattern requires a $180°$ constant phase shift between the
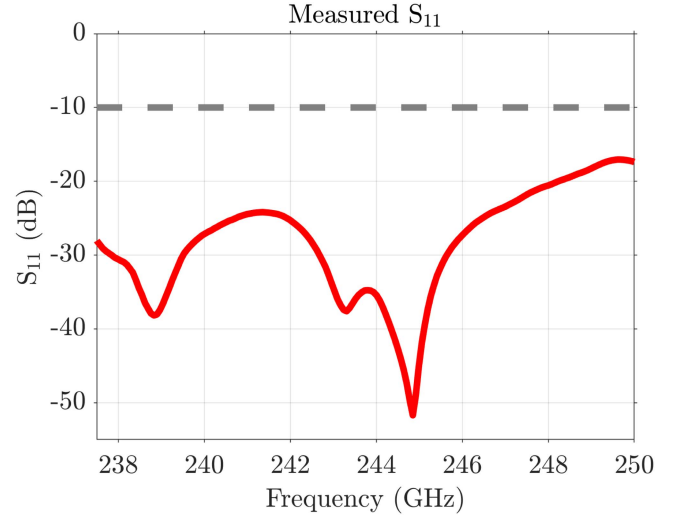
Fig. 3. Measured S_{11} of the radar frontend in the notch-beam. As can be seen, the input port is perfectly matched within the frequency range of 237.5–250 GHz.

Fig. 4. Measured radiation patterns of the radar frontend at different frequencies in the E-plane, showing the steerable notch pattern.

two antenna elements, which is implemented by a magic-tee. The antenna array is fed by the delta port of the magic-tee, whose outputs are connected via a delay-line network to the dual-element antenna, designed to achieve beam-steering from

(a)

(b)

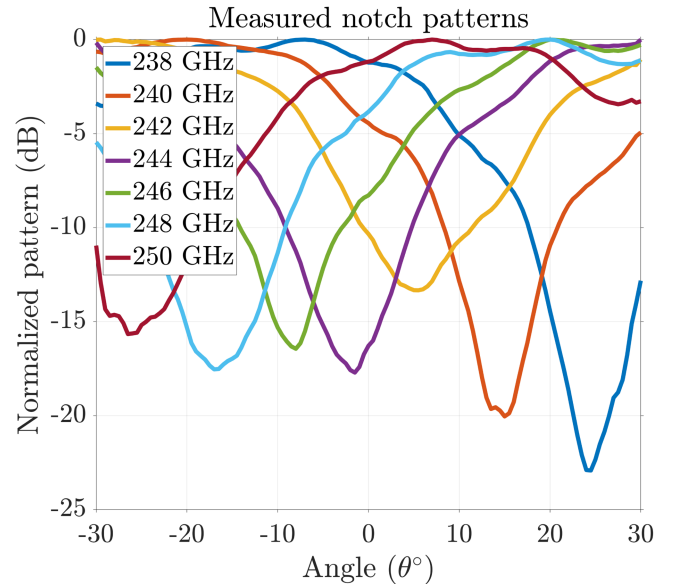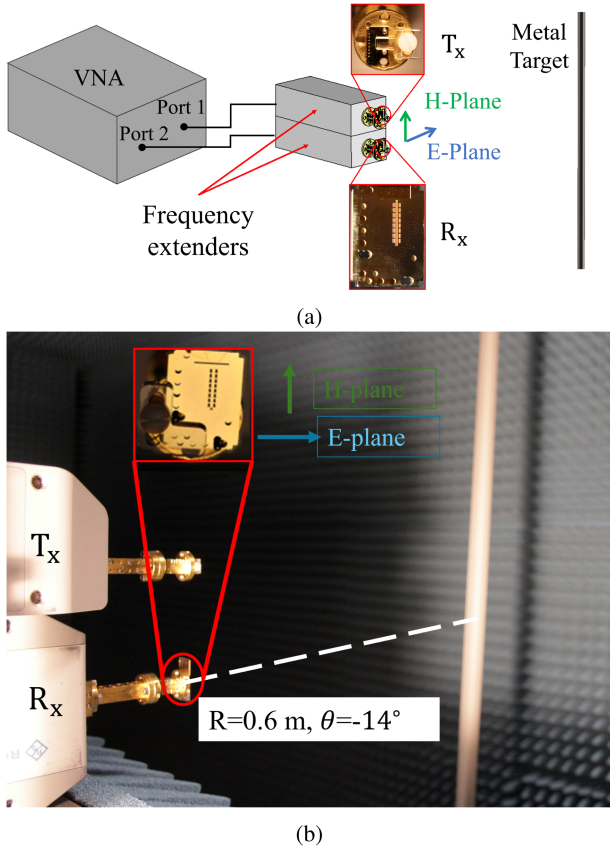Fig. 5.   (a) Schematic view of the measurement setupt. (b) Measurement setup for the single-target measurement. Tx and Rx antennas are positioned vertically.

$-26.5°$ to $28°$ for an operating bandwidth of 12.5 GHz, spanning from 237.5 to 250 GHz.

The antenna array comprises two unbalanced corporate-fed single-line (1×8) subarrays with reduced sidelobe level in the H-plane. The length difference of the feeding lines is $12\lambda_c$ at the center frequency, inducing a frequency-dependent phase shift between the subarrays required for beam-steering. The utilized delay line network creates more than $\pm 90°$ of phase difference by sweeping the frequency from 237.5 to 250 GHz.

The beam-steering frontend has a standard WR-3.4 rectangular waveguide interface, enabling the direct connection of the fabricated frontend prototype to other system components.

III. SIGNAL PROCESSING

A pivotal aspect of designing radar systems is the selection of suitable signal-processing techniques that align with the hardware's capabilities. The utilized antenna array's unique characteristics significantly influence signal-processing algorithms' efficiency, potentially reducing computational load. To comprehensively investigate the proposed frequency scanning notch beam radar system, the performance of three advanced algorithms—MF, FISTA, and MUSIC—is evaluated. These algorithms, each with different levels of complexity and approaches, are selected for two primary reasons: first, to verify

the functionality of the radar, and second, to determine which algorithm is best suited to this hardware.

Advancements in compressed sensing algorithms have markedly enhanced radar computational imaging, offering a significant leap forward from conventional methodologies, such as time reversal or the fast Fourier transform. These advanced approaches unlock the potential for more efficient and effective radar imaging, setting a new standard for processing techniques in the field and requiring higher computational complexity. The following standard formulation summarizes the essence of compressed sensing:

$$\mathbf{y} = \mathbf{K}\mathbf{x} + \mathbf{w} \tag{7}$$

where $\mathbf{x}$ represents a signal vector of length N in R^N, and $\mathbf{y}$ is a compressed signal vector of length M in R^M, with $M \ll N$. The matrix $\mathbf{K}$, the compressed sensing (measurement) matrix, encapsulated the transformation from $\mathbf{x}$ to $\mathbf{y}$, incorporating both the incident and reflected electrical corresponding to each pixel of the discretized FoV as in (8), and $\mathbf{w}$ is an added Gaussian noise to the signal. Equation (8) explains how to fill up matrix $\mathbf{K}$

$$\mathbf{K} = [K_{mn}]_{M \times N}, \ K_{mn} = \frac{e^{-jk_m r_n} E^i_{mn}}{4\pi r_n} \times \frac{e^{-jk_m r_n} E^r_{mn}}{4\pi r_n}. \tag{8}$$

E^i and E^r represent the incident and reflected electrical fields, respectively. In (9) and (8), indices m and n denote the mth measurement (specifically, the mth frequency sample) and the nth pixel within the FoV, respectively. In addition, k_m signifies the wave number associated with the mth measurement and r_n indicates the distance from the radar to the nth pixel. Utilizing the first Born approximation and using the first term of the Taylor expansion, the coupling between pixels is neglected. The reflected signal of each pixel is the multiplication of the incident field and the reflection coefficient of each pixel. The maximum normalized reflection coefficient to perfect electric conductors (PEC) is 1. Thus, for the PEC target, the reflected and incident waves are equal

$$E^i_{mn} = E^r_{mn}, \ K_{mn} = \left(\frac{e^{-jk_m r_n} E^i_{mn}}{4\pi r_n} \right)^2. \tag{9}$$

A. Matched Filter

MF technique is widely used in radar signal processing to maximize the signal-to-noise ratio (SNR). This method enhances the detectability of the radar by correlating the received signal with a template of the expected signal [30]. For a given radar inverse problem as (7), the MF provides the least square solution using the following equation:

$$\hat{\mathbf{x}} = \mathbf{K}'\mathbf{y} \tag{10}$$

where $\mathbf{K}'$ is the adjoint matrix of $\mathbf{K}$, and $\hat{\mathbf{x}}$ is a least square approximation of $\mathbf{x}$.
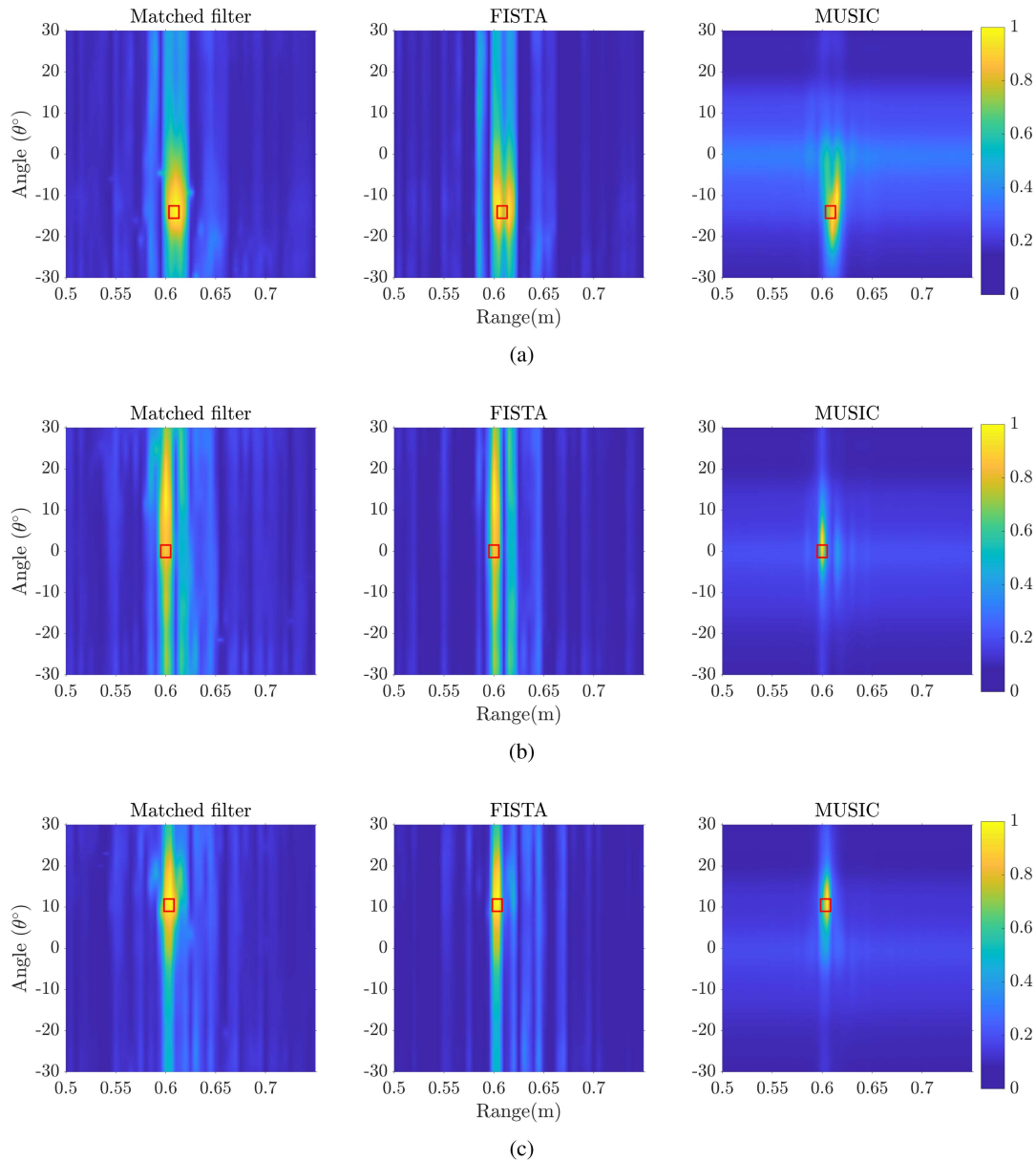
Fig. 6. Single-target scene reconstructed images: targets positioned at 0.6 ± 0.01 m and (a) $-14°$, (b) $0°$, (c) $+10.5°$.

B. Fast Iterative-Shrinkage Thresholding Algorithm

FISTA enhances the recovery of sparse signals using an accelerated gradient method, surpassing traditional IST algorithms through iterative updates that include gradient steps, shrinkage/thresholding, and updates of auxiliary variables [22]. The efficiency of FISTA, particularly its rapid convergence when compared to ISTA, is attributed to the introduction of the auxiliary variable and an ingenious update mechanism that leverages information from previous iterations.

C. MUSIC Method

As a super-resolution technique, the MUSIC algorithm excels in signal processing applications for estimating the direction of arrival of multiple sources. By employing the eigenvalue decomposition of the data covariance matrix, MUSIC differentiates the signal subspace associated with the sources, enabling precise estimation of the direction of arrival angles [21]. This capability is invaluable in scenarios with closely spaced sources or low SNR conditions, highlighting the algorithm's versatility and power in radar and array processing applications.

In the proposed radar system, with only one transmit (Tx) and one receive (Rx) antenna, the MUSIC algorithm's capability is inherently limited. Specifically, the maximum number of correctly detectable targets is $n - 1$, where n is the total number of antennas. Therefore, with the single Tx and Rx configuration, the maximum number of correctly detectable targets is one.

IV. RADAR PERFORMANCE CHARACTERIZATION

The experiments are performed in an anechoic antenna measurement chamber operable within 67–750 GHz [31]. The
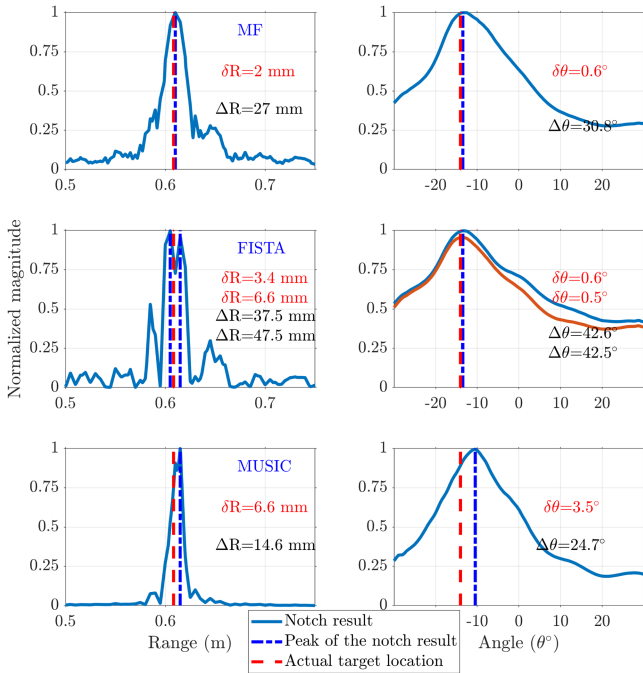
Fig. 7.   Range and angular distribution of the reconstructed images of the first scene signal-target scenario for the three algorithms.
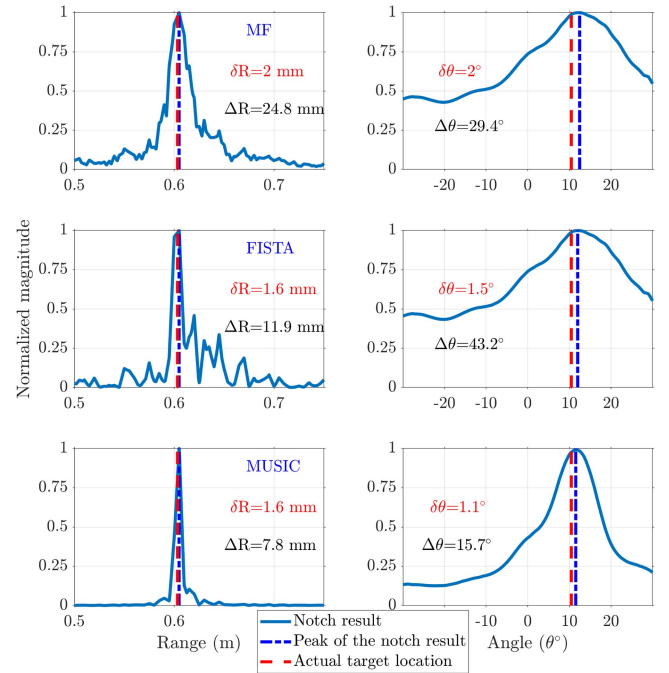

Fig. 9.   Range and angular distribution of the reconstructed images of the third scene signal-target scenario for the three algorithms.
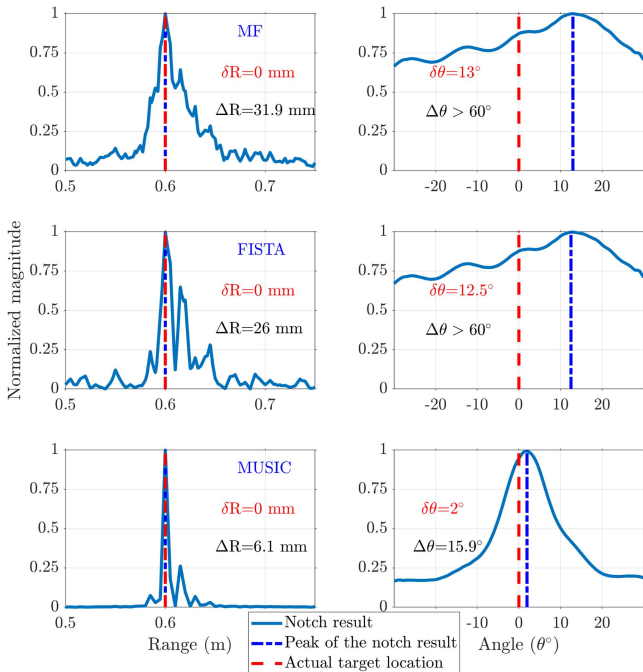

Fig. 8.   Range and angular distribution of the reconstructed images of the second scene signal-target scenario for the three algorithms.

TABLE II
DETECTION PERFORMANCES OF THE ALGORITHMS FOR DUAL-TARGET SCENES

Parameters	Algorithms	Target 1	Target 2
	MF	0	0
Range error (δR mm)	FISTA	4.7	5
	MUSIC	4.7	5
	MF	4.5	3
Angle error ($\delta\theta°$)	FISTA	4.5	2.5
	MUSIC	3.5	9

chamber is equipped with a 4-degree-of-freedom fully automated robot and is covered with high-frequency absorbers to minimize reflections, facilitating accurate radiation pattern measurements. The S-parameters and patterns are measured using a Rohde and Schwarz ZVA-24 Vector Network Analyzer with ZC-330 frequency extenders operating in the 220–330 GHz.

The measurement setup is calibrated with a standard calibration kit using the through-offset-short-match method, shifting the measurement reference planes to the surface of the waveguide flanges right at the radar frontends input port. The measured S_{11} is presented in Fig. 3.

The measured notch radiation patterns in the E-plane are shown in Fig. 4. The beams are measured with $0.5°$ steps in the E-plane and $0.25°$ steps in the H-plane and are averaged and normalized over a $1°$ angle (five E-plane cuts) due to the distributed nature of the targets in the scene. The HPBW in the H-plane radiation patterns was characterized and is between $8.5°$ and $9.5°$ [12] in the steering range.

The beam-steering frontend is first evaluated by single-target measurements, focusing on characterizing range and angular accuracy, and then by dual-target scenarios for characterizing the target discrimination capability.

An schematic view and experimental configuration of the single-target measurement setup are depicted in Fig. 5. Given the frontend's narrow beamwidth in the H-plane, positioning the Tx and Rx antennas as shown in Fig. 5 minimizes the coupling between them, increasing the network analyzer's dynamic range. In these measurements, one frequency extender operates as the
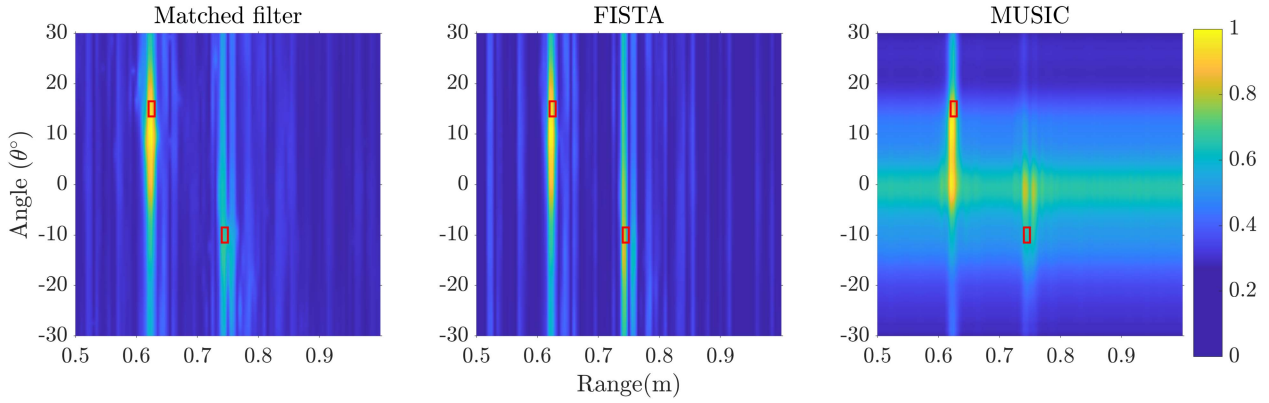
Fig. 10. Dual-target scene reconstructed images: targets positioned in range at 0.62 ± 0.01 m and 0.74 ± 0.01 m from the center of the Tx/Rx, encompassing three distinct angles: $15°$, $-10°$.
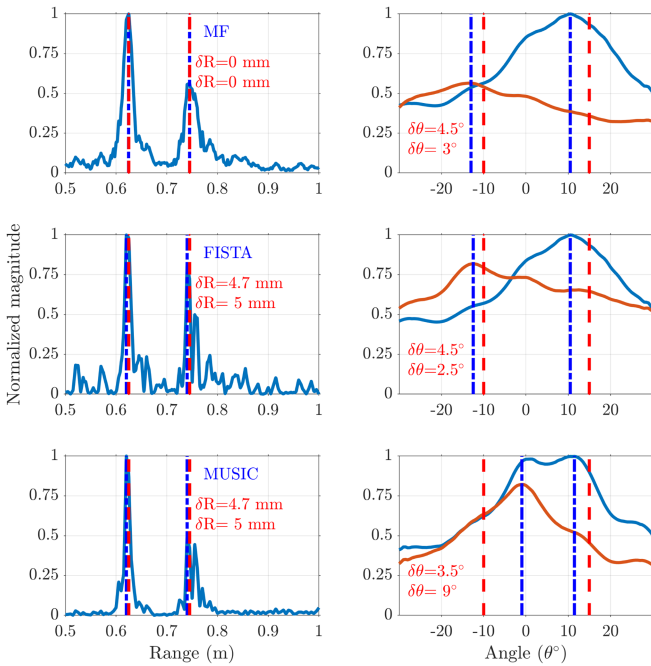

Fig. 11. Range and angular distribution of the reconstructed images of the dual-target scene: targets positioned in range at 0.62 ± 0.01 m and 0.74 ± 0.01 m from the center of the Tx/Rx, encompassing two distinct angles: $15°$, $-10°$.

transmitter and is connected to a 1×8 antenna array with a broad fan beam over the steering range [12]. The other frequency extender, which acts as the receiver, is connected to the antenna under test, i.e., the radar frontend prototype. The angular and range resolutions, $\Delta\theta$ and ΔR, respectively, are defined as the width of the reconstructed image's range and angular distributions at -3 dB from the peaks. The detection errors, δR and $\delta\theta$, represent the deviation of the detected values from the actual values.

A. Single-Target Measurements

Three single-target scenarios were investigated to assess the radar frontend performance in detecting and localizing a target at different angles. The target is a vertically long corner metal

with 4 cm sides to enhance the SNR. At a distance of 0.6 m, the angular size of the target is approximately $5.34°$. Due to the size of the target, the target was assumed at a distance of 0.6 ± 0.01 m from the receiver (the phase center of the target would vary according to the target geometry and angle) centered at three distinct angles: $0°$, $-14°$, and $+10.5°$. The imaging scene is discretized into range and angular bins of 5 mm and $0.5°$, respectively, covering a range from 0.5 to 0.75 m and $\pm30°$ FoV, totaling in $N = 51 \times 121 = 6171$ pixels, and a total of $M = 201$ frequency measurement samples were taken, (7) is classified as an underdetermined convex problem.

The target's actual location in the results is marked by a black dashed line, indicating the center of the target.

The 2-D reconstructed images for these three single-target scenarios by the MF, FISTA, and MUSIC algorithms are displayed in Fig. 6.

The first single-target scenario is the target positioned 0.6 m away and aligned at $-14°$. Reconstructed images from the measurement data, presented in Fig. 6(a) and 7, illustrate the system's capacity for target visualization. The three algorithms were able to successfully detect and localize the target with a range error of less than 6.6 mm and angular error of below $3.5°$, which are smaller values compared to the physical dimension of the target. MUSIC offers higher range resolution $\Delta R = 14.6$ mm close to the range resolution for the nonscanning broad beam $\Delta R = 12.5$ mm and angular resolution $\Delta\theta = 24.7°$. Notably, the range resolution for MF and FISTA are compatible with the nature of the frequency sweeping beam scanning and effective bandwidth discussed in Section II [16]. On the other hand, the MUSIC, as a super-resolution algorithm, provides higher range resolution. Moreover, due to the wide notch-beam, the angular resolution results in low angular resolution with a wide distribution.

Fig. 6(b) displays the reconstructed image of a target situated at a distance of 0.6 m and an angle of $0°$. This visualization in Fig. 8 underscores the effectiveness of the three algorithms under consideration.

Notably, the MUSIC algorithm demonstrated superior range resolution $\Delta R = 6.1$ mm without range error, reaffirming its

status as a super-resolution technique. Also, in angular resolution, MUSIC offers angular resolution $\Delta\theta = 15.9°$ with angular error $2°$ that is less than the physical angular size of the target. MF and FISTA achieved range resolutions comparable to the first scene with zero range error. However, they did not present meaningful angular information. This failure in accurate angular detection is attributed to the poor notch depth at angular ranges from $\theta = 0°$ to $\theta = 10°$.

The reconstructed images of the third target scenario, illustrated in Fig. 6(c) at a distance of 0.6 m and an angle of $+10.5°$, showcase the precision with which the algorithms can detect range and angular information.

The range and angular distribution of the reconstructed images for this scenario in Fig. 9 highlights the superior performance of the MUSIC algorithm in single-target scenarios.

A comprehensive summary of the findings for the single-target experiments is provided in Table I. This table offers a unified perspective on the comparative performance of the algorithms under various test conditions. The red values in the table show that the angular detection error for MF and FISTA in the second scenario is larger than the angular size of the target.

B. Dual-Target Measurements

Three dual-target experiments were conducted to evaluate the radar system's efficiency in detecting and localizing multiple targets. Due to the similarity in scenarios and results, only one dual-target experiment is presented here.

The targets were strategically positioned at distances of 0.62 ± 0.01 and 0.74 ± 0.01 m from the radar's center, spanning angles of $15°$, and $-10°$. The targets are the same as single target tests, and the target's angular sizes are $5.15°$, $4.33°$.

The imaging scene is discretized into range and angular bins of 5 mm and $0.5°$, respectively, covering a range from 0.5 to 1 m and $\pm30°$. The scene has $N = 101\times121 = 12\,221$ pixels, and the total frequency measurement samples is $M = 201$. The results of dual-target tests are shown in Fig. 10, which represents 2-D reconstructed images, and Fig. 11, which illustrates the range and angular distribution of the two detected targets. In contrast to single-target measurements, the MUSIC algorithm only detected one of the targets in the dual-target scenario, while MF and FISTA detected both targets with angular errors of below $3°$.

It can be concluded that MUSIC outperforms MF and FISTA in single-target scenarios, but in multitarget cases, MUSIC fails to provide acceptable angular resolution.

The localization performance of each algorithm when confronted with dual-target scenarios is concisely captured in Table II, which provides detailed information on the range and angular detection errors, illustrating the performance of each algorithm in navigating the complexities of multitarget configurations. The red value in the table shows that the angular detection error for MUSIC is larger than the angular size of the target.

V. CONCLUSION

This article thoroughly investigates a radar frontend designed in the sub-THz range, specifically between 237.5 and 250 GHz.

The radar frontend utilizes a two-line antenna array and advanced silicon micromachining fabrication techniques to implement a frequency-scanning notch-beam covering an angular scan from $-26.5°$ to $28°$. Moreover, the effectiveness of the MUSIC, MF, and FISTA algorithms in different measurement scenarios was analyzed. The MUSIC algorithm demonstrated superior range and angular resolutions in single-target scenarios, aligning with its super-resolution capabilities. However, its performance is limited in multitarget scenarios due to the inherent restriction in the number of correctly detectable targets. In contrast, despite offering weaker resolution, the MF and FISTA algorithms proved to be more robust in multitarget scenarios. This robustness is due to their different data processing techniques, making them less affected by the limitations faced by the MUSIC algorithm.

REFERENCES

[1] D. Sheen, D. McMakin, and T. Hall, "Three-dimensional millimeter-wave imaging for concealed weapon detection," *IEEE Trans. Microw. Theory Techn.*, vol. 49, no. 9, pp. 1581–1592, Sep. 2001, doi: 10.1109/22.942570.

[2] I. Walterscheid, J. Ender, A. Brenner, and O. Loffeld, "Bistatic SAR processing and experiments," *IEEE Trans. Geosci. Remote Sens.*, vol. 44, no. 10, pp. 2710–2717, Oct. 2006, doi: 10.1109/TGRS.2006.881848.

[3] J. Hasch et al., "Millimeter-wave technology for automotive radar sensors in the 77 GHz frequency band," *IEEE Trans. Microw. Theory Techn.*, vol. 60, no. 3, pp. 845–860, Mar. 2012, doi: 10.1109/TMTT.2011.2178427.

[4] M. Pauli et al., "Miniaturized millimeter-wave radar sensor for high-accuracy applications," *IEEE Trans. Microw. Theory Techn.*, vol. 65, no. 5, pp. 1707–1715, May 2017, doi: 10.1109/TMTT.2017.2677910.

[5] A. Arbabian, S. Callender, S. Kang, M. Rangwala, and A. M. Niknejad, "A 94 GHz mm-Wave-to-baseband pulsed-radar transceiver with applications in imaging and gesture recognition," *IEEE J. Solid-State Circuits*, vol. 48, no. 4, pp. 1055–1071, Apr. 2013, doi: 10.1109/JSSC.2013.2239004.

[6] K. B. Cooper et al., "THz imaging radar for standoff personnel screening," *IEEE Trans. THz Sci. Technol.*, vol. 1, no. 1, pp. 169–182, Sep. 2011, doi: 10.1109/TTHZ.2011.2159556.

[7] A. Gomez-Torrent et al., "A 38 dB gain, low-loss, flat array antenna for 320–400 GHz enabled by silicon-on-insulator micromachining," *IEEE Trans. Antennas Propag.*, vol. 68, no. 6, pp. 4450–4458, Jun. 2020, doi: 10.1109/TAP.2020.2969753.

[8] R. C. Hansen, *Microwave Scanning Antennas*, vol. 1. New York, NY, USA: Academic, 1964.

[9] M. Danielsen and R. Jorgensen, "Frequency scanning microstrip antennas," *IEEE Trans. Antennas Propag.*, vol. AP-27, no. 2, pp. 146–150, Mar. 1979, doi: 10.1109/TAP.1979.1142049.

[10] A. Karimi, U. Shah, and J. Oberhammer, "Sub-THz silicon-micromachined reconfigurable beam-steering frontend," in *Proc. 53rd Eur. Microw. Conf.*, 2023, pp. 448–451, doi: 10.23919/EuMC58039.2023.10290347.

[11] K. Sarabandi, A. Jam, M. Vahidpour, and J. East, "A novel frequency beam-steering antenna array for submillimeter-wave applications," *IEEE Trans. THz Sci. Technol.*, vol. 8, no. 6, pp. 654–665, Nov. 2018, doi: 10.1109/TTHZ.2018.2866019.

[12] A. Karimi, U. Shah, A. Madannejad, and J. Oberhammer, "Silicon-micromachined subterahertz frequency beam-steered dual-port array antenna," *IEEE Trans. THz Sci. Technol.*, vol. 14, no. 2, pp. 258–268, Mar. 2024, doi: 10.1109/TTHZ.2023.3344023.

[13] M. S. Rabbani, J. Churm, and A. P. Feresidis, "Continuous beam-steering low-loss millimeter-wave antenna based on a piezo-electrically actuated metasurface," *IEEE Trans. Antennas Propag.*, vol. 70, no. 4, pp. 2439–2449, Apr. 2022, doi: 10.1109/TAP.2021.3137248.

[14] Z. L. Ma, K. B. Ng, C. H. Chan, and L. J. Jiang, "A novel supercell-based dielectric grating dual-beam leaky-wave antenna for 60-GHz applications," *IEEE Trans. Antennas Propag.*, vol. 64, no. 12, pp. 5521–5526, Dec. 2016, doi: 10.1109/TAP.2016.2621031.

[15] S. M. Sherman and D. K. Barton, *Monopulse Principles and Techniques*. Norwood, MA, USA: Artech House, 2011.

[16] M.-R. Seidi, U. Shah, and J. Oberhammer, "Analysis of a minimalistic imaging radar concept employing beam shape switching and compressed sensing," *IEEE Trans. Geosci. Remote Sens.*, vol. 62, 2024, Art. no. 2003812, doi: 10.1109/TGRS.2024.3383223.

[17] A. Madannejad, M. M. Gohari, U. Shah, and J. Oberhammer, "High-gain circularly polarized 500–750 GHz lens antenna enabled by silicon micromachining," *IEEE Trans. Antennas Propag.*, vol. 72, no. 5, pp. 4077–4085, May 2024, doi: 10.1109/TAP.2024.3383289.

[18] B. Beuerle, J. Campion, U. Shah, and J. Oberhammer, "A very low loss 220–325 GHz silicon micromachined waveguide technology," *IEEE Trans. THz Sci. Technol.*, vol. 8, no. 2, pp. 248–250, Mar. 2018, doi: 10.1109/TTHZ.2018.2791841.

[19] C. Jung-Kubiak et al., "A multistep DRIE process for complex terahertz waveguide components," *IEEE Trans. THz Sci. Technol.*, vol. 6, no. 5, pp. 690–695, Sep. 2016, doi: 10.1109/TTHZ.2016.2593793.

[20] A. Gomez-Torrent et al., "A low-profile and high-gain frequency beam steering subterahertz antenna enabled by silicon micromachining," *IEEE Trans. Antennas Propag.*, vol. 68, no. 2, pp. 672–682, Feb. 2020, doi: 10.1109/TAP.2019.2943328.

[21] R. Schmidt, "Multiple emitter location and signal parameter estimation," *IEEE Trans. Antennas Propag.*, vol. AP-34, no. 3, pp. 276–280, Mar. 1986, doi: 10.1109/TAP.1986.1143830.

[22] A. Beck and M. Teboulle, "A fast iterative shrinkage-thresholding algorithm for linear inverse problems," *SIAM J. Imag. Sci.*, vol. 2, no. 1, pp. 183–202, 2009, doi: 10.1137/080716542.

[23] S. Li et al., "Near-field radar imaging via compressive sensing," *IEEE Trans. Antennas Propag.*, vol. 63, no. 2, pp. 828–833, Feb. 2015, doi: 10.1109/TAP.2014.2381262.

[24] M. Wang et al., "Lightweight FISTA-inspired sparse reconstruction network for mmW 3-D holography," *IEEE Trans. Geosci. Remote Sens.*, vol. 60, 2022, Art. no. 5211620, doi: 10.1109/TGRS.2021.3093307.

[25] T.-H. Chou, N. Michelusi, D. J. Love, and J. V. Krogmeier, "Compressed training for dual-wideband time-varying sub-terahertz massive MIMO," *IEEE Trans. Commun.*, vol. 71, no. 6, pp. 3559–3575, Jun. 2023, doi: 10.1109/TCOMM.2023.3247789.

[26] S. Razavian, S. Thomas, M. Hosseini, and A. Babakhani, "Micro-doppler detection and vibration sensing using silicon-based THz radiators," *IEEE Sensors J.*, vol. 22, no. 14, pp. 14091–14101, Jul. 2022, doi: 10.1109/JSEN.2022.3183002.

[27] W. Hu et al., "Ultra-wideband signal generation and fusion algorithm for high-resolution terahertz FMCW radar imaging," *Opt. Exp.*, vol. 30, no. 6, pp. 9814–9822, Mar. 2022, doi: 10.1364/OE.450985.

[28] W. Hu et al., "High-resolution range profile reconstruction method for terahertz fmcw radar," *Appl. Opt.*, vol. 60, no. 22, pp. 6400–6408, Aug. 2021, doi: 10.1364/AO.431232.

[29] M. Soumekh, Synthetic Aperture Radar Signal Processing With MATLAB Algorithms. Hoboken, NJ, USA: Wiley, 1999.

[30] G. Turin, "An introduction to matched filters," *IRE Trans. Inf. Theory*, vol. 6, no. 3, pp. 311–329, 1960, doi: 10.1109/TIT.1960.1057571.

[31] A. Madannejad, M. M. Gohari, U. Shah, and J. Oberhammer, "High-gain circularly polarized 500–750 GHz lens antenna enabled by silicon micromachining," *IEEE Trans. Antennas Propag.*, vol. 72, no. 5, pp. 4077–4085, May 2024.

Mohammad-Reza Seidi (Graduate Student Member, IEEE) was born in Tehran, Iran. He received the bachelor's degree in electrical engineering focused on communication engineering from the K. N. Toosi University of Technology, Tehran, Iran, in 2015 and the master's degree in electrical engineering focused on applied electromagnetic engineering from the University of Tehran, Tehran, Iran, in 2019. He is currently working toward the Ph.D. degree with the KTH Royal Institute of Technology, Stockholm, Sweden.

The main focus of his studies was metamaterial application in radar and imaging systems. His research interests include radar and imaging systems, antenna design, RF components, and lectromagnetic wave propagation.

Armin Karimi (Member, IEEE) was born in Kermanshah, Iran, in 1993. He received the B.Sc. degree in electrical engineering, focusing on communication systems and the M.Sc. degree in applied electromagnetics, fields, and waves from the University of Tehran, Tehran, Iran, in 2016 and 2019, respectively, and the Ph.D. degree in silicon micromachined terahertz and subterahertz components and systems with the Division of Micro and Nano Systems, KTH Royal Institute of Technology, Stockholm, Sweden, in 2024.

His research interests are applied electromagnetics, RF-MEMS, nanofabrication, microwave and mm-wave active and passive components, array antenna, filter, imaging systems, metamaterial and metasurface, and signal chain design.

Dr. Karimi was a recipient of the Young Engineer Award at European Microwave Week 2023, Berlin, Germany, and the Best Student Paper Award presented at Swedish Microwave Days 2023, Stockholm.

Alireza Madannejad (Graduate Student Member, IEEE) was born in Iran in 1992. He received the M.Sc. degree in electrical engineering from the University of Tehran, Tehran, Iran, in 2017. He is currently working toward the Ph.D. degree with the Division of Micro and Nano Systems, KTH Royal Institute of Technology, Stockholm, Sweden.

In 2017, he was a technical staff and Researcher with the Antenna Type Approval Lab, University of Tehran. He has worked in applied electromagnetics, antenna, and component measurement, telecommunications systems, and radar systems. Since 2021, he has been working on the THz communication system and passive component design.

Umer Shah (Senior Member, IEEE) was born in Bannu, Pakistan, in 1981. He received the B.S. degree in engineering from the Ghulam Ishaq Khan Institute of Engineering Sciences and Technology, Topi, Pakistan, in 2003, the M.Sc. degree in wireless engineering from the Technical University of Denmark, Kgs. Lyngby, Denmark, in 2007, and the Ph.D. degree in microsystem technology from the KTH Royal Institute of Technology, Stockholm, Sweden, in 2014.

Since 2014, he has been a Researcher with the Division of Micro and Nanosystems, KTH Royal Institute of Technology. He has authored or coauthored more than 50 reviewed papers. His research interests include millimeter-wave and Terahertz filters, phase shifters, matching circuits, and antennas. This includes utilizing MEMS reconfigurability to achieve tunability at millimeter-wave and terahertz frequencies.

Joachim Oberhammer (Senior Member, IEEE) born in Italy in 1976. He received the M.Sc. degree in electrical engineering from the Graz University of Technology, Graz, Austria, in 2000 and the Ph.D. degree from the KTH Royal Institute of Technology, Stockholm, Sweden, in 2004.

He was a Postdoctoral Research Fellow with Nanyang Technological University, Singapore, in 2004, and Kyoto University, Kyoto, Japan, in 2008. Since 2005, he has been leading radio frequency/microwave/terahertz microelectromechanical systems research with the KTH Royal Institute of Technology; an Associate Professor with the KTH Royal Institute of Technology in 2010, and a Professor in Microwave and THz Microsystems with the KTH Royal Institute of Technology, since 2015. He was a Guest Researcher with Nanyang Technological University in 2007, a Guest Researcher at NASA-Jet Propulsion Laboratory, Pasadena, CA, USA, in 2014, and a Guest Professor "Chair of Excellence" at Universidad Carlos III de Madrid, Madrid, Spain, in 2019 and 2020.